Statistical Modeling of Underwater Wireless Channels

Alenka G. Zajić
School of Computer Science
Georgia Institute of Technology, Atlanta, GA 30332 USA

***Abstract*— This paper proposes a geometry-based statistical model for multiple-input multiple-output shallow water wireless channels. From the reference model, the corresponding space-time-frequency correlation function and space-Doppler power spectral density are derived. To verify our results, the derived statistics are compared with the experimentally obtained channel statistics and close agreement is observed.**

I. Introduction

Shallow water acoustic (SWA) wireless communications find applications in oceanographic data collection, tactical surveillance, assisted navigation, pollution monitoring, and offshore exploration. To make these applications feasible, there is a need for statistical characterization of the acoustic wireless communication channel. The SWA wireless channel is one of the most challenging wireless communication channels. First obstacle is the fact that acoustic signals propagate through water at a very low speed (1500 $\mathrm{m/s}$). Furthermore, they suffer from attenuation that depends not only on the distance but also on the signal frequency. In addition, the acoustic signals are greatly affected by the reflections from the ocean surface and ocean floor and by variations in the speed of sound at different water depths. All these variations in the medium cause the path-dependent Doppler and angle spreading, which results in a time-varying wideband channel impulse response with long delay spreads [1]-[3]. Together, these factors produce a communication medium that combines the worst of radio worlds: poor link quality of a terrestrial system and high latency of a satellite system.

Addressing the challenges in underwater wireless communications requires statistical characterization of acoustic wireless communication channels. While there exist several deterministic and statistical simulation models for SWA wireless channels [4]-[9], a statistical framework for SWA channels, i.e., correlation functions, Doppler power spectral density, power delay spectral density, etc., is still an open problem. These statistics are necessary tools for a proper design and analysis of multiple-input multiple-output (MIMO) SWA communication systems. Furthermore, the closed-form expressions of these statistics can be useful for estimation of physical parameters such as angle spread, mean angles of departure and arrival, etc. By taking into account only macro-scattering effects, Abdi and Guo [10] were the first to derive the space-frequency correlation function for *time-invariant* isovelocity SWA channels.

In contrast, this paper models a *time-varying* SWA channel by taking into account both macro- and micro-scattering effects. We first introduce a new geometry-based statistical model for wideband MIMO SWA multipath fading channels. The proposed model characterizes the sound propagation in shallow water isovelocity environments by combining the deterministic ray-tracing theory with the statistical methods needed to characterize the random components of the propagation medium. From the statistical model, the corresponding space-time-frequency correlation function (stf-cf) and space-Doppler power spectral density (sD-psd) for a shallow water isovelocity environment are derived. Finally, to illustrate the utility of the proposed model, we compare the temporal correlation function and sD-psd with those obtained from measurements in [11].

The remainder of the paper is organized as follows. Section II introduces the geometry-based statistical model for wideband MIMO SWA multipath fading channels. Section III derives the stf-cf and the sD-psd for a shallow water isovelocity environment. Section IV compares the analytical and measured results for the temporal correlation function and the sD-psds. Finally, Section V provides some concluding remarks.

II. Geometry-based Statistical Model for Wideband MIMO SWA Channels

This paper considers a MIMO communication system with L_t transmit and L_r receive transducers. The propagation occurs in shallow water environments with constant sound speed, i.e., sound energy propagates along the plane waves. The propagation is characterized with either line-of-sight or non-line-of-sight conditions between the transmitter ($\mathrm{T_x}$) and the receiver ($\mathrm{R_x}$). The MIMO SWA channel can be described by an $L_r \times L_t$ matrix $\mathbf{P}(t,\tau) = [P_{ij}(t,f)]_{L_r \times L_t}$ of the time-varying transfer functions.

Fig. 1 shows a SWA channel with $L_t = L_r = 2$ transducer elements. This elementary 2×2 transducer configuration will be used later to construct uniform linear arrays with an arbitrary number of transducer elements. The SWA channel is modeled as a two-dimensional (2-D) waveguide bounded from the top and the bottom. The surface and bottom boundaries reflect an acoustic signal, which results in multiple rays travelling between the $\mathrm{T_x}$ and $\mathrm{R_x}$, as shown in Fig. 1. The roughness of sea surface and sea bottom is characterized by S and B macro-scatterers, respectively. At any time instance t, the $\mathrm{R_x}$ receives $2S$ downward arriving rays, each one having different number of s surface and b bottom reflections, where

$1 \leq s \leq S$, and $s-1 \leq b \leq s$. Similarly, there are $2B$ upward arriving rays with b bottom and s surface reflections, where $1 \leq b \leq B$ and $b-1 \leq s \leq b$. Note that the exact positions of scatterers depend on the surface and bottom characteristics and may vary from one location to another and from one time instance to another. On the other hand, the average of scattering positions over different locations (or time instances) depends only on the waveguide geometry and the number of rays and can be computed. To implement this idea, each ray is modeled as an average of micro-rays scattered from N_{sb} possible positions of surface scatterers and M_{bs} possible positions of bottom scatterers (i.e., micro-scatterers), where the possible positions of scatterers are clustered around the averaged positions of scatterers (i.e., macro-scatterers), as shown in Fig. 1. The horizontal spacing between the $\mathrm{T_x}$ and

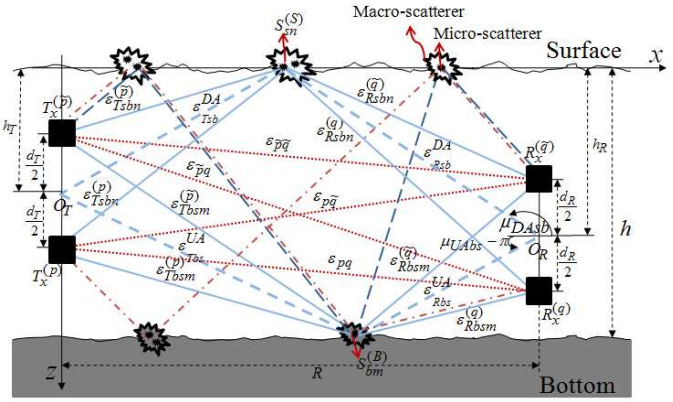

Fig. 1. The geometry-based model for MIMO wideband SWA channels with $L_t = L_r = 2$ transducer elements.

$\mathrm{R_x}$ is denoted by R. The water depth is denoted by h, while the depths of $\mathrm{T_x}$ and $\mathrm{R_x}$ are denoted by h_T and h_R, respectively. As we are interested in medium and long range shallow water communications, we assume that the depths h, h_T, and h_R are much smaller than the distance R. The spacing between two adjacent transducer elements at the $\mathrm{T_x}$ and $\mathrm{R_x}$ is d_T and d_R, respectively. It is assumed that d_T and d_R are much smaller than the depths h, h_T, and h_R. The symbols $\epsilon^{(p)}_{Tsbn}$ and $\epsilon^{(p)}_{Tbsm}$ denote distances $T_x^{(p)}$-$S_{sn}^{(S)}$ and $T_x^{(p)}$-$S_{bm}^{(B)}$, respectively, where $S_{sn}^{(S)}$ and $S_{bm}^{(B)}$ denote the n^{th} and m^{th} micro-scatterers at the surface and bottom, respectively, for $1 \leq n \leq N_{tb}$ and $1 \leq m \leq M_{bt}$, as shown in Fig. 1. Similarly, the symbols $\epsilon^{(\tilde{p})}_{Tsbn}$, $\epsilon^{(\tilde{p})}_{Tbsm}$, $\epsilon^{(q)}_{Rsbn}$, $\epsilon^{(q)}_{Rbsm}$, $\epsilon^{(\tilde{q})}_{Rsbn}$, $\epsilon^{(\tilde{q})}_{Rbsm}$, ϵ_{pq}, $\epsilon_{\tilde{p}q}$, $\epsilon_{p\tilde{q}}$, and $\epsilon_{\tilde{p}\tilde{q}}$ denote distances $T_x^{(\tilde{p})}$-$S_{sn}^{(S)}$, $T_x^{(\tilde{p})}$-$S_{bm}^{(B)}$, $S_{sn}^{(S)}$-$R_x^{(q)}$, $S_{bm}^{(B)}$-$R_x^{(q)}$, $S_{sn}^{(S)}$-$R_x^{(\tilde{q})}$, $S_{bm}^{(B)}$-$R_x^{(\tilde{q})}$, $T_x^{(p)}$-$R_x^{(q)}$, $T_x^{(\tilde{p})}$-$R_x^{(q)}$, $T_x^{(p)}$-$R_x^{(\tilde{q})}$, and $T_x^{(\tilde{p})}$-$R_x^{(\tilde{q})}$, respectively. For ease of reference, Fig. 2 details the geometry of the deterministic propagation paths (DPP) as well as the geometry of single-bounced surface and single-bounced bottom rays (i.e., $s=1, b=0$, $s=0, b=1$) scattered from the n^{th} and m^{th} micro-scatterers, respectively. Angles θ_T and θ_R in Fig. 2 describe the orientations of $\mathrm{T_x}$ and $\mathrm{R_x}$ transducer arrays in the x-z plane, respectively, relative to the x-axis. The $\mathrm{T_x}$ and $\mathrm{R_x}$ are moving with constant speeds v_T and v_R in directions described by angles γ_T and γ_R in the x-z plane (relative to the x-axis), respectively. The symbols $\alpha^{(p)}_{Tsbn}$ and $\alpha^{(p)}_{Tbsm}$ are the angles of departure (AoD) of rays that start from $T_x^{(p)}$ and impinge on the scatterers $S_{sn}^{(S)}$ and $S_{bm}^{(B)}$, respectively, whereas $\alpha^{(q)}_{Rsbn}$ and $\alpha^{(q)}_{Rbsm}$ are the angles of arrival (AoA) of the rays scattered from $S_{tn}^{(S)}$ and $S_{bm}^{(B)}$ and arriving at $R_x^{(q)}$, respectively. Finally, the symbols α_{Rdpp} and D_{dpp} denote the AoA of DPP ray and the distance O_T-O_R, respectively.

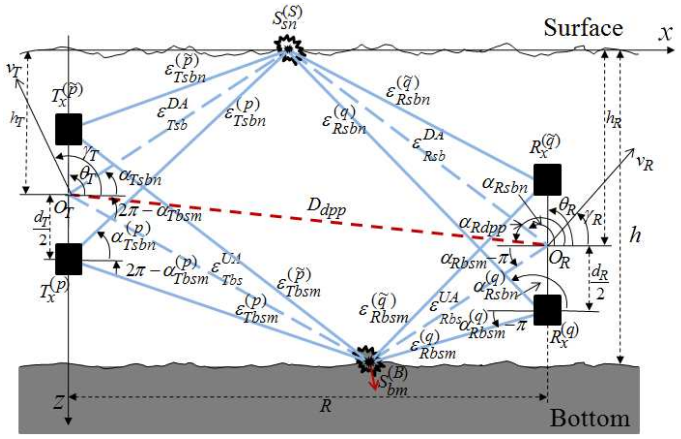

Fig. 2. The detailed geometry of the DPP, single-bounced surface, and single-bounced bottom rays scattered from the n^{th} and m^{th} micro-scatterer, respectively.

Observe from the geometrical model in Fig. 1 that propagation through SWA channel can be characterized as a superposition of surface-bottom bounced rays and the DPP ray between the $\mathrm{T_x}$ and $\mathrm{R_x}$. The multiple bounced rays can be grouped into the upward arriving (UA) rays (i.e., the last reflection is from the bottom) and the downward arriving (DA) rays (i.e., the last reflection is from the surface). Then, the time-varying transfer function of the pressure link $T_x^{(p)}$-$R_x^{(q)}$ can be written as a superposition of the DPP, UA, and DA rays, viz.

$$P_{pq}(t,f) = P_{pq}^{DPP}(t,f) + P_{pq}^{UA}(t,f) + P_{pq}^{DA}(t,f). \quad (1)$$

The DPP component of the time-varying transfer function is

$$P_{pq}^{DPP}(t,f) = \sqrt{\frac{K}{K+1}} e^{-j2\pi f \tau_{dpp}^{(p,q)}(t)}, \quad (2)$$

where K is the Rice factor (ratio of DPP to scatter received power) and $\tau_{dpp}^{(p,q)}(t)$ is the DPP time delay (the travel time of the direct ray between $T_x^{(p)}$ and $R_x^{(q)}$) i.e.,

$$\tau_{dpp}^{(p,q)}(t) = \frac{\epsilon_{pq}}{c} - \frac{v_T}{c} t\cos(\alpha_{Rdpp} - \gamma_T) + \frac{v_R}{c} t\cos(\alpha_{Rdpp} - \gamma_R), \quad (3)$$

where c is the speed of sound. The upward and downward arriving components of the time-varying transfer function are,

respectively,

$$P_{pq}^{UA}(t,f) = \sqrt{\frac{\eta_B}{2B(K+1)}}\sqrt{\frac{1}{M_{bs}}} \sum_{b=1}^{B}\sum_{s=b-1}^{b}\sum_{m=1}^{M_{bs}} \xi_{bsm} e^{j\phi_{bsm}} e^{-j2\pi f \tau_{bsm}^{(p,q)}(t)}, \quad (4)$$

$$P_{pq}^{DA}(t,f) = \sqrt{\frac{\eta_S}{2S(K+1)}}\sqrt{\frac{1}{N_{sb}}} \sum_{s=1}^{S}\sum_{b=s-1}^{s}\sum_{n=1}^{N_{sb}} \xi_{sbn} e^{j\phi_{sbn}} e^{-j2\pi f \tau_{sbn}^{(p,q)}(t)}, \quad (5)$$

where $\xi_{bsm} > 0$ and $\xi_{sbn} > 0$ denote the amplitudes and ϕ_{bsm} and ϕ_{sbn} denote the phases of multipath components. The time delays $\tau_{bsm}^{(p,q)}(t)$ and $\tau_{sbn}^{(p,q)}(t)$ are the travel times of UA and DA rays with s surface and b bottom reflections, respectively, i.e.,

$$\tau_{sbn}^{(p,q)}(t) = \frac{D_{sb}^{DA}}{c} - \frac{\epsilon_{Tsb}^{DA} - \epsilon_{Tsbn}^{(p)}}{c} - \frac{\epsilon_{Rsb}^{DA} - \epsilon_{Rsbn}^{(q)}}{c} + \frac{1}{c}\Delta Z_{sbn}(t)\sin\alpha_{Rsbn}^{(q)} + \frac{1}{c}\left[v_T t\cos(\alpha_{Tsbn}^{(p)} - \gamma_T) + v_R t\cos(\alpha_{Rsbn}^{(q)} - \gamma_R)\right], \quad (6)$$

$$\tau_{bsm}^{(p,q)}(t) = \frac{D_{bs}^{UA}}{c} - \frac{\epsilon_{Tbs}^{UA} - \epsilon_{Tbsm}^{(p)}}{c} - \frac{\epsilon_{Rbs}^{UA} - \epsilon_{Rbsm}^{(q)}}{c} + \frac{1}{c}\Delta Z_{bsm}(t)\sin\alpha_{Rbsm}^{(q)} + \frac{1}{c}\left[v_T t\cos(\alpha_{Tbsm}^{(p)} - \gamma_T) + v_R t\cos(\alpha_{Rbsm}^{(q)} - \gamma_R)\right], \quad (7)$$

where $\Delta Z_{sbn}(t)$ and $\Delta Z_{bsm}(t)$ denote the vertical displacements of surface scatterers due to the surface motion and the distances ϵ_{Tsb}^{DA}, ϵ_{Rsb}^{DA}, ϵ_{Tbs}^{UA}, and ϵ_{Rbs}^{UA} denote distances O_T-$S_{sn}^{(S)}$, $S_{sn}^{(S)}$-O_R, O_T-$S_{bm}^{(B)}$, $S_{bm}^{(B)}$-O_R, as shown in Fig. 1. Finally, D_{bs}^{UA} and D_{sb}^{DA} denote the total distances travelled by UA and DA rays with s surface and b bottom reflections. These distances are obtained using the method of images [12] and can be approximated as

$$D_{sb}^{DA} \approx \frac{2}{R}[b^2h^2 + bhh_R - (-1)^{(s-b)}bhh_T + (s-b)h_Th_R], \quad (8)$$

$$D_{bs}^{UA} \approx \frac{2}{R}[s^2h^2 - shh_R + (-1)^{(b-s)}shh_T + (b-s)h_Th_R]. \quad (9)$$

It is assumed that the AoDs ($\alpha_{Tsbn}^{(p)}$ and $\alpha_{Tbsm}^{(p)}$), the AoAs ($\alpha_{Rsbn}^{(q)}$ and $\alpha_{Rbsm}^{(q)}$), and the vertical displacements $\Delta Z_{sbn}(t)$ and $\Delta Z_{bsm}(t)$ are random variables. Furthermore, it is assumed that the phases ϕ_{sbn} and ϕ_{bsm} are uniform random variables on the interval $[-\pi, \pi)$ that are independent from the AoDs, the AoAs, and the vertical displacements at the surface. Using the assumptions introduced above and the Central Limit Theorem [13], we can conclude that $h_{pq}^{UA}(t,\tau)$ and $h_{pq}^{DA}(t,\tau)$ are independent complex Gaussian random processes with zero means. Note that the AoDs ($\alpha_{Tsbn}^{(p)}$ and $\alpha_{Tbsm}^{(p)}$) are dependent on the AoAs ($\alpha_{Rsbn}^{(q)}$ and $\alpha_{Rbsm}^{(q)}$), respectively. Assuming small angle spreads, $d_T \ll \min(h_T, h - h_T)$, and $d_R \ll \min(h_R, h - h_R)$, we can approximate the AoDs and AoAs in Fig. 2 as $\alpha_{Tsbn}^{(p)} \approx \alpha_{Tsbn}^{(\tilde{p})} \approx \alpha_{Tsbn}$, $\alpha_{Tbsm}^{(p)} \approx \alpha_{Tbsm}^{(\tilde{p})} \approx \alpha_{Tbsm}$, $\alpha_{Rsbn}^{(q)} \approx \alpha_{Rsbn}^{(\tilde{q})} \approx \alpha_{Rsbn}$, and $\alpha_{Rbsm}^{(q)} \approx \alpha_{Rbsm}^{(\tilde{q})} \approx \alpha_{Rbsm}$, where α_{Tsbn}, α_{Tbsm}, α_{Rsbn}, and α_{Rbsm} are shown in Fig. 2. Assuming that each ray, when interacting with the surface and bottom, has equal incident and reflecting angles, we can observe that $\alpha_{Tsbn} = \pi - \alpha_{Rsbn}$ and $\alpha_{Tbsm} = 3\pi - \alpha_{Rbsm}$.

The distances $\epsilon_{Tsbn}^{(p)}$, $\epsilon_{Tbsm}^{(p)}$, $\epsilon_{Rsbn}^{(q)}$, $\epsilon_{Rbsm}^{(q)}$, and ϵ_{pq} can be expressed as functions of the random angles α_{Rsbn} and α_{Rbsm} and the angle α_{Rdpp} as follows

$$\epsilon_{Tsbn}^{(p)} \approx \frac{h_T}{\sin\alpha_{Rsbn}} + \frac{L_t + 1 - 2p}{2} d_T\cos(\alpha_{Rsbn} + \theta_T) \quad (10)$$

$$\epsilon_{Tbsm}^{(p)} \approx -\frac{h - h_T}{\sin\alpha_{Rbsm}} + \frac{L_t + 1 - 2p}{2} d_T\cos(\alpha_{Rbsm} + \theta_T) \quad (11)$$

$$\epsilon_{Rsbn}^{(q)} \approx \frac{h_R}{\sin\alpha_{Rsbn}} - \frac{L_r + 1 - 2q}{2} d_R\cos(\alpha_{Rsbn} - \theta_R) \quad (12)$$

$$\epsilon_{Rbsm}^{(q)} \approx -\frac{h - h_R}{\sin\alpha_{Rbsm}} - \frac{L_r + 1 - 2q}{2} d_R\cos(\alpha_{Rbsm} - \theta_R) \quad (13)$$

$$\epsilon_{pq} \approx 0.5(L_t + 1 - 2p)d_T\cos(\alpha_{Rdpp} - \theta_T) - 0.5(L_r + 1 - 2q)d_R\cos(\alpha_{Rdpp} - \theta_R), \quad (14)$$

where parameters p and q take values from the sets $p \in \{1, \ldots, L_t\}$ and $q \in \{1, \ldots, L_r\}$, respectively. The derivations of approximations in (10)-(14) are omitted for brevity. Finally, we note that ϵ_{Tsb}^{DA}, ϵ_{Rsb}^{DA}, ϵ_{Tbs}^{UA}, and ϵ_{Rbs}^{UA} can be written as functions of the mean AoA angles μ_{DAsb} and μ_{UAbs}, i.e., $\epsilon_{Tsb}^{DA} = h_T/\sin\mu_{DAsb}$, $\epsilon_{Rsb}^{DA} = h_R/\sin\mu_{DAsb}$, $\epsilon_{Tbs}^{UA} = -(h - h_T)/\sin\mu_{UAbs}$, and $\epsilon_{Rbs}^{UA} = -(h - h_R)/\sin\mu_{UAbs}$, where the AoA angles μ_{DAsb} and μ_{UAbs} are depicted in Fig. 1.

The angles of arrival α_{Rsbn} and α_{Rbsm} are modeled using the following Gaussian probability density functions (pdfs)

$$f_{\text{top}}(\alpha_{Rsbn}) = \frac{1}{\sqrt{2\pi\sigma_{DAsb}^2}}\exp\left\{-\frac{(\alpha_{Rsbn} - \mu_{DAsb})^2}{(2\sigma_{DAsb}^2)}\right\}, \quad \text{for } 0 < \alpha_{Rsbn} < \pi, \quad (15)$$

$$f_{\text{bottom}}(\alpha_{Rbsm}) = \frac{1}{\sqrt{2\pi\sigma_{UAbs}^2}}\exp\left\{-\frac{(\alpha_{Rbsm} - \mu_{UAbs})^2}{(2\sigma_{UAbs}^2)}\right\} \quad \text{for } \pi < \alpha_{Rbsm} < 2\pi, \quad (16)$$

where μ_{DAsb} and μ_{UAbs} are the mean AoAs, whereas σ_{DAsb} and σ_{UAbs} are the angle spreads.

Finally, the vertical displacements $\Delta Z_{sbn}(t)$ and $\Delta Z_{bsm}(t)$ are modeled as zero-mean Gaussian random processes with stationary and independent increments and can be written as

$$f(\Delta Z_{sbn}(t)) = \frac{1}{\sqrt{2\pi t\zeta_{\Delta Z_{DAsb}}^2}}\exp\left\{-\frac{(\Delta Z_{sbn}(t))^2}{(2t\zeta_{\Delta Z_{DAsb}}^2)}\right\}, \quad (17)$$

$$f(\Delta Z_{bsm}(t)) = \frac{1}{\sqrt{2\pi t\zeta_{\Delta Z_{UAbs}}^2}}\exp\left\{-\frac{(\Delta Z_{bsm}(t))^2}{(2t\zeta_{\Delta Z_{UAbs}}^2)}\right\}, \quad (18)$$

where $t\zeta_{\Delta Z_{DAsb}}^2$ and $t\zeta_{\Delta Z_{UAbs}}^2$ denote the variances.

III. Space-Time-Frequency Correlation Function and Space-Doppler Power Spectrum of the Statistical Model

Assuming a 2-D wide sense stationary uncorrelated scattering (WSSUS) isovelocity shallow water environment, we first derive the stf-cf of the geometry-based statistical model. From the stf-cf, we derive the corresponding sD-psd.

The normalized stf-cf between two time-variant transfer functions $P_{pq}(t,f)$ and $P_{\tilde{p}\tilde{q}}(t+\Delta t, f+\Delta f)$, is defined as

$$R_{pq,\tilde{p}\tilde{q}}(\Delta t,\Delta f)=\frac{\mathrm{E}\left[P_{pq}(t,f)^{*}P_{\tilde{p}\tilde{q}}(t+\Delta t,f+\Delta f)\right]}{\sqrt{\mathrm{E}[|P_{pq}(t,f)|^2]\mathrm{E}[|P_{\tilde{p}\tilde{q}}(t,f)|^2]}}, \quad (19)$$

where $(\,\cdot\,)^{*}$ denotes complex conjugate operation, $\mathrm{E}[\,\cdot\,]$ is the statistical expectation operator, $p,\tilde{p}\in\{1,\ldots,L_t\}$, and $q,\tilde{q}\in\{1,\ldots,L_r\}$. Since $P_{pq}^{UA}(t,f)$ and $P_{pq}^{DA}(t,f)$ are independent zero-mean random processes, (19) can be simplified to

$$\begin{aligned} R_{pq,\tilde{p}\tilde{q}}(\Delta t,\Delta f) &= R_{pq,\tilde{p}\tilde{q}}^{DPP}(\Delta t,\Delta f) \quad (20)\\ &+ R_{pq,\tilde{p}\tilde{q}}^{UA}(\Delta t,\Delta f)+R_{pq,\tilde{p}\tilde{q}}^{DA}(\Delta t,\Delta f), \end{aligned}$$

where $R_{pq,\tilde{p}\tilde{q}}^{DPP}(\Delta t,\Delta f)$, $R_{pq,\tilde{p}\tilde{q}}^{UA}(\Delta t,\Delta f)$, and $R_{pq,\tilde{p}\tilde{q}}^{DA}(\Delta t,\Delta f)$ denote the normalized stf-cfs of the DPP, UA, and DA components, respectively. Substituting (2) into (20), the expression for the stf-cf of DPP component can be written as

$$\begin{aligned} &R_{pq,\tilde{p}\tilde{q}}^{DPP}(\Delta t,\Delta f)=K/(K+1)\\ &e^{j\frac{2\pi}{\lambda}[v_T\Delta t\cos(\alpha_{Rdpp}-\gamma_T)-v_R\Delta t\cos(\alpha_{Rdpp}-\gamma_R)]}\\ &e^{j\frac{2\pi}{\lambda}[(p-\tilde{p})d_T\cos(\alpha_{Rdpp}-\theta_T)-(q-\tilde{q})d_R\cos(\alpha_{Rdpp}-\theta_R)]}, \quad (21) \end{aligned}$$

where λ denotes the carrier wavelength. Similarly, substituting (4) and (5) into (20), noting that the phases ϕ_{bsm} and ϕ_{sbn} are independent and uniformly distributed over $[-\pi,\pi)$, assuming that $M_{bs}\gg 1$ and $N_{sb}\gg 1$, using the first-order Taylor expansion for the AoD and AoA angles, and using the equality $\int e^{j\alpha x}(2\pi\sigma^2)^{-1/2}e^{-x^2/(2\sigma^2)}dx=e^{-\sigma^2\alpha^2/2}$ [10], the stf-cfs of UA and DA components can be closely approximated as

$$\begin{aligned} &R_{pq,\tilde{p}\tilde{q}}^{UA}(\Delta t,\Delta f)=\frac{\eta_B}{2B(K+1)}\sum_{b=1}^{B}\sum_{s=b-1}^{b}e^{-\frac{\Delta t\zeta_{\Delta Z_{UAbs}}^2}{2}[\frac{2\pi}{\lambda}\sin\mu_{UAbs}]^2}\\ &e^{-j\frac{2\pi\Delta f}{c}D_{bs}^{UA}+j\frac{2\pi}{\lambda}[(p-\tilde{p})d_T\cos(\mu_{UAbs}+\theta_T)-(q-\tilde{q})d_R\cos(\mu_{UAbs}-\theta_R)]}\\ &e^{j\frac{2\pi}{\lambda}[v_T\Delta t\cos(\mu_{UAbs}+\gamma_T)-v_R\Delta t\cos(\mu_{UAbs}-\gamma_R)]-\frac{\sigma_{UAbs}^2}{2}X_{UAbs}^2}, \quad (22)\\ &R_{pq,\tilde{p}\tilde{q}}^{DA}(\Delta t,\Delta f)=\frac{\eta_S}{2S(K+1)}\sum_{s=1}^{S}\sum_{b=s-1}^{s}e^{-\frac{\Delta t\zeta_{\Delta Z_{DAsb}}^2}{2}[\frac{2\pi}{\lambda}\sin\mu_{DAsb}]^2}\\ &e^{-j\frac{2\pi\Delta f}{c}\tilde{D}_{sb}^{DA}+j\frac{2\pi}{\lambda}[(q-\tilde{q})d_R\cos(\mu_{DAsb}-\theta_R)-(p-\tilde{p})d_T\cos(\mu_{DAsb}+\theta_T)]}\\ &e^{j\frac{2\pi}{\lambda}[v_T\Delta t\cos(\mu_{DAsb}+\gamma_T)-v_R\Delta t\cos(\mu_{DAsb}-\gamma_R)]-\frac{\sigma_{DAsb}^2}{2}X_{DAsb}^2}, \quad (23) \end{aligned}$$

where $X_{UAbs}=\frac{2\pi\Delta f}{c}\frac{h_R+h_T-2h}{\sin\mu_{UAbs}\tan\mu_{UAbs}}+\frac{2\pi}{\lambda}[(q-\tilde{q})d_R\sin(\mu_{UAbs}-\theta_R)-(p-\tilde{p})d_T\sin(\mu_{UAbs}+\theta_T)]+\frac{2\pi}{\lambda}[v_R\Delta t\sin(\mu_{UAbs}-\gamma_R)-v_T\Delta t\sin(\mu_{UAbs}+\gamma_T)]+\Delta t\zeta_{\Delta Z_{UAbs}}^2[\frac{2\pi}{\lambda}]^2\sin\mu_{UAbs}\cos\mu_{UAbs}$,
$X_{DAsb}=\frac{2\pi\Delta f}{c}\frac{h_R+h_T}{\sin\mu_{DAsb}\tan\mu_{DAsb}}+\frac{2\pi}{\lambda}[(q-\tilde{q})d_R\sin(\mu_{DAsb}-\theta_R)-(p-\tilde{p})d_T\sin(\mu_{DAsb}+\theta_T)]+\frac{2\pi}{\lambda}[v_R\Delta t\sin(\mu_{DAsb}-\gamma_R)-v_T\Delta t\sin(\mu_{DAsb}+\gamma_T)]+\Delta t\zeta_{\Delta Z_{DAsb}}^2[\frac{2\pi f_c}{c}]^2\sin\mu_{DAsb}\cos\mu_{DAsb}$.

The sD-psd of the time-variant transfer function is the Fourier transform of the space-time correlation function $R_{pq,\tilde{p}\tilde{q}}(\Delta t,\Delta f=0)$. From (20), it follows that the sD-psd is a summation of the sD-psd functions of the DPP, UA, and DA components, i.e.,

$$S_{pq,\tilde{p}\tilde{q}}(\nu)=S_{pq,\tilde{p}\tilde{q}}^{DPP}(\nu)+S_{pq,\tilde{p}\tilde{q}}^{UA}(\nu)+S_{pq,\tilde{p}\tilde{q}}^{DA}(\nu). \quad (24)$$

By calculating the Fourier transform of the stf-cf in (21), we obtain the sD-psd of the DPP component as follows

$$\begin{aligned} &S_{pq,\tilde{p}\tilde{q}}^{DPP}(\nu)=e^{j\frac{2\pi}{\lambda}[(p-\tilde{p})d_T\cos(\alpha_{Rdpp}-\theta_T)-(q-\tilde{q})d_R\cos(\alpha_{Rdpp}-\theta_R)]}\\ &\frac{K}{K+1}\delta\Big(\nu-\frac{v_R}{\lambda}\cos(\alpha_{Rdpp}-\gamma_R)+\frac{v_T}{\lambda}\cos(\alpha_{Rdpp}-\gamma_T)\Big). \quad (25) \end{aligned}$$

Similarly, by calculating the Fourier transforms of the stf-cfs in (22) and (23) and using the equality $\int_{-\infty}^{\infty}\exp\{-p^2x^2\pm qx\}dx=\exp\{q^2/(4p^2)\}\sqrt{\pi}/p$ [14, eq. 3.323-2], we obtain the sD-psds of the UA and DA components, respectively,

$$\begin{aligned} &S_{pq,\tilde{p}\tilde{q}}^{UA}(\nu)=\frac{\eta_B}{2B(K+1)}\sum_{b=1}^{B}\sum_{s=b-1}^{b}e^{-\frac{\sigma_{UAbs}^2}{2}B_{UAbs}^2}\\ &e^{\frac{\left(j2\pi\nu+C_{UAbs}+0.5\sigma_{UAbs}^2A_{UAbs}B_{UAbs}\right)^2}{\sigma_{UAbs}^4A_{UAbs}^2}}\frac{\sqrt{\pi}}{0.5\sigma_{UAbs}^2A_{UAbs}}\\ &e^{j\frac{2\pi}{\lambda}[(p-\tilde{p})d_T\cos(\mu_{UAbs}+\theta_T)-(q-\tilde{q})d_R\cos(\mu_{UAbs}-\theta_R)]}, \quad (26)\\ &S_{pq,\tilde{p}\tilde{q}}^{DA}(\nu)=\frac{\eta_S}{2S(K+1)}\sum_{s=1}^{S}\sum_{b=s-1}^{s}e^{-\frac{\sigma_{DAsb}^2}{2}B_{DAsb}^2}\\ &e^{\frac{\left(j2\pi\nu+C_{DAsb}+0.5\sigma_{DAsb}^2A_{DAsb}B_{DAsb}\right)^2}{\sigma_{DAsb}^4A_{DAsb}^2}}\frac{\sqrt{\pi}}{0.5\sigma_{DAsb}^2A_{DAsb}}\\ &e^{j\frac{2\pi}{\lambda}[(p-\tilde{p})d_T\cos(\mu_{DAsb}+\theta_T)-(q-\tilde{q})d_R\cos(\mu_{DAsb}-\theta_R)]}, \quad (27) \end{aligned}$$

where A_{UAbs}, B_{UAbs}, C_{UAbs}, A_{DAsb}, B_{DAsb}, and C_{DAsb} are

$$\begin{aligned} &A_{UAbs}=\zeta_{\Delta Z_{UAbs}}^2\left[\frac{2\pi}{\lambda}\right]^2\sin\mu_{UAbs}\cos\mu_{UAbs}\\ &+2\pi\left[v_R\sin(\mu_{UAbs}-\gamma_R)-v_T\sin(\mu_{UAbs}+\gamma_T)\right]/\lambda, \quad (28)\\ &B_{UAbs}=-2\pi(p-\tilde{p})d_T\sin(\mu_{UAbs}+\theta_T)/\lambda\\ &+2\pi(q-\tilde{q})d_R\sin(\mu_{UAbs}-\theta_R)/\lambda, \quad (29)\\ &C_{UAbs}=\frac{\zeta_{\Delta Z_{UAbs}}^2}{2}\left[\frac{2\pi}{\lambda}\sin\mu_{UAbs}\right]^2\\ &+j2\pi\left[v_R\cos(\mu_{UAbs}-\gamma_R)-v_T\cos(\mu_{UAbs}+\gamma_T)\right]/\lambda, \quad (30)\\ &A_{DAsb}=\zeta_{\Delta Z_{DAsb}}^2\left[\frac{2\pi}{\lambda}\right]^2\sin\mu_{DAsb}\cos\mu_{DAsb}\\ &+2\pi[v_R\sin(\mu_{DAsb}-\gamma_R)-v_T\sin(\mu_{DAsb}+\gamma_T)]/\lambda, \quad (31)\\ &B_{DAsb}=-2\pi(p-\tilde{p})d_T\sin(\mu_{DAsb}+\theta_T)/\lambda\\ &+2\pi(q-\tilde{q})d_R\sin(\mu_{DAsb}-\theta_R)/\lambda, \quad (32)\\ &C_{DAsb}=\frac{\zeta_{\Delta Z_{DAsb}}^2}{2}\left[\frac{2\pi}{\lambda}\sin\mu_{DAsb}\right]^2\\ &+j2\pi\left[v_R\cos(\mu_{DAsb}-\gamma_R)-v_T\cos(\mu_{DAsb}+\gamma_T)\right]/\lambda. \quad (33) \end{aligned}$$

IV. Comparison with Measured Data

In this section, we compare the theoretical results in Section III with the AUVFest07 measured data in [11], collected

at calm sea. The close agreement between the analytical and measured statistics is observed.

The channel measurements in [11] are collected at $f_c = 17$ kHz and the speed of sound was $c = 1470$ m/s. The distance between the $\mathrm{T_x}$ and $\mathrm{R_x}$ was $R = 5$ km. The water, $\mathrm{T_x}$, and $\mathrm{R_x}$ depths were $h = 20$ m, $h_T = 19$ m, and $h_R = 18$ m, respectively. The $\mathrm{T_x}$ and $\mathrm{R_x}$ are equipped with vertically oriented transducer elements (i.e., $\theta_T = \theta_R = 90^\circ$). It is assumed that the $\mathrm{T_x}$ and $\mathrm{R_x}$ are relatively stationary, i.e., slightly moving with waves (i.e., $\gamma_T = \gamma_R = 90^\circ$).

Fig. 3 compares the analytical temporal correlation function with the measured temporal correlation function. Furthermore, Fig. 4 compares the analytical and measured sD-psds. The analytical curves in Figs. 3 and 4 are obtained with the parameters $K = 0.8$, $S = B = 1$, $v_T = 0.0006$ m/s, $v_R = 0.00025$ m/s, $\zeta_{\Delta Z_{DA10}} = \zeta_{\Delta Z_{DA11}} = 0.0097$, $\zeta_{\Delta Z_{UA10}} = \zeta_{\Delta Z_{UA11}} = 0.0087$, $\mu_{DA10} = 169^\circ$, $\mu_{DA11} = 167^\circ$, $\mu_{UA10} = 194^\circ$, $\mu_{UA11} = 195^\circ$, $\sigma_{DA10} = 3.25^\circ$, $\sigma_{DA11} = 5^\circ$, $\sigma_{UA10} = 2.7^\circ$, $\sigma_{UA11} = 3.2^\circ$, $\eta_S = 0.28$, and $\eta_B = 1 - \eta_S$. The Rice factor K is estimated using the moment-method in [15], and the parameters S and B are visually estimated from Fig. 3a in [11]. The rest of the parameters, i.e., $[v_T, v_R, \zeta_{\Delta Z_{DAsb}}, \zeta_{\Delta Z_{UAbs}}, \mu_{DAsb}, \mu_{UAbs}, \sigma_{DAsb}, \sigma_{UAbs}, \eta_S]$ are estimated jointly using the maximum-likelihood approach in [16] and the constraint $\eta_S + \eta_B = 1$.

The close agreement between the analytical and measured statistics in Figs. 3 and 4 confirms the utility of the derived statistics.

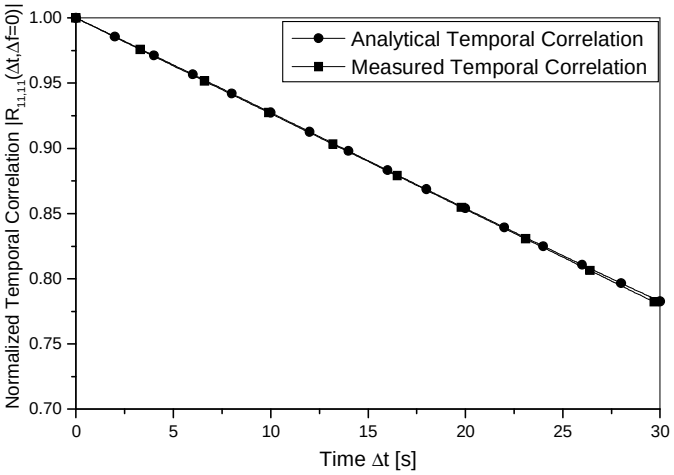

Fig. 3. The magnitudes of analytical and measured temporal correlation functions.

V. Conclusions

This paper proposed the geometry-based statistical model for MIMO SWA fading channels. From the statistical model, the corresponding space-time-frequency correlation function and space-Doppler power spectral density are derived. Finally, the derived statistics are compared with the experimentally obtained channel statistics and the close agreement is observed.

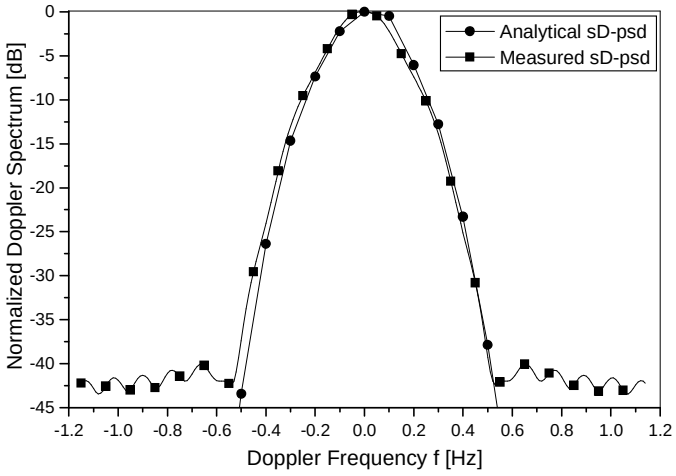

Fig. 4. The normalized analytical and measured space-Doppler power spectral density.

References

[1] M. Stojanovic, "Recent advances in high-speed underwater acoustic communications," *IEEE Journal of Oceanic Eng.*, vol. 21, pp. 125–136, Apr. 1996.

[2] T. B. Aik, Q. S. Sen, and Z. Nan, "Characterization of multipath acoustic channels in very shallow waters for communications," *Proc. OCEANS'06 Asia-Pacific*, Singapore, May 2007.

[3] M. Badiey, Y. Mu, J. A. Simmen, and S. E. Forsythe, "Signal variability in shallow-water sound channels," *IEEE Journal of Oceanic Eng.*, vol. 25, pp. 492–500, Oct. 2000.

[4] D. B. Kilfoyle and A. B. Baggeroer, "The state of the art in underwater acoustic telemetry," *IEEE Journal of Oceanic Eng.*, vol. 25, pp. 4–27, Jan. 2000.

[5] R. H. Owen, B. V. Smith, and R. F. W. Coates, "An experimental study of rough surface scattering and its effects on communication coherence," c

[6] A. Essebbar, G. Loubet, and F. Vial, "Underwater acoustic channel simulations for communication," *Proc. OCEANS'94*, vol. 3, pp. 495–500, Brest, France, Sept. 1994.

[7] A. Zielinski, Y-H. Yoon, and L. Wu, "Performance analysis of digital acoustic communication in a shallow water channel," *IEEE Journal of Oceanic Eng.*, vol. 20, pp. 293–299, Oct. 1995.

[8] C. Bjerrum-Niese, L. Bjorno, M. A. Pinto, and B. Quellec, "A simulation tool for high data-rate acoustic communication in a shallow-water, time-varying channel," *IEEE Journal of Oceanic Eng.*, vol. 21, pp. 143–149, Apr. 1996.

[9] M. Chitre, "A high-frequency warm shallow water acoustic communications channel model and measurements," *J. Acoust. Soc. Am.*, vol. 122, pp. 2580–2586, Nov. 2007.

[10] A. Abdi and H. Guo, "Signal correlation modeling in acoustic vector sensor arrays," *IEEE Transactions on Signal Processing*, vol. 57, pp. 892–903, Mar. 2009.

[11] T. C. Yang, "Toward continuous underwater acoustic communications,"*Proc. OCEANS'08*, Quebec City, Canada, Sept. 2008.

[12] L. M. Brekhovskikh and Y. Lysanov, *Fundamentals of ocean acoustics 2e*. Springer, Berlin, 1991.

[13] G. L. Stüber, *Principles of mobile communication 2e.*Kluwer, 2001.

[14] I. S. Gradshteyn and I. M. Ryzhik, *Table of Integrals, Series, and Products* . San Diego, CA, 5th ed., 1994.

[15] L. J. Greenstein, D. G. Michelson, and V. Erceg, "Moment-method estimation of the Ricean K-factor," *IEEE Commun. Letters*, vol. 3, pp. 175–176, June 1999.

[16] A. G. Zajić, G. L. Stüber, T. G. Pratt, and S. Nguyen, "Wideband mimo mobile-to-mobile channels: geometry-based statistical modeling with experimental verification," *IEEE Trans. Veh. Tech.*, vol. 58, pp. 517-534, Feb. 2009.